EXPERIMENTAL AND NUMERICAL STUDIES ON TURBULENCE STRUCTURES IN WAKE OF WALL-MOUNTED FINITE SQUARE CYLINDER IN TURBULENT BOUNDARY LAYER OF VISCOELASTIC FLUIDS

Shinji Tamano
Graduate School of Engineering
Nagoya Institute of Technology
Gokiso-cho, Showa-ku, Nagoya, Aichi 466-8555, JAPAN
tamano.shinji@nitech.ac.jp

Ryuga Sumi
Graduate School of Engineering
Nagoya Institute of Technology
Gokiso-cho, Showa-ku, Nagoya, Aichi 466-8555, JAPAN
r.sumi.505@stn.nitech.ac.jp

Ayato Yokoi
Graduate School of Engineering
Nagoya Institute of Technology
Gokiso-cho, Showa-ku, Nagoya, Aichi 466-8555, JAPAN
a.yokoi.715@stn.nitech.ac.jp

Masakazu Muto
Graduate School of Engineering
Nagoya Institute of Technology
Gokiso-cho, Showa-ku, Nagoya, Aichi 466-8555, JAPAN
muto.masakazu@nitech.ac.jp

ABSTRACT

Some kinds of polymer and surfactant solutions have viscoelastic properties and cause significant frictional drag reduction in wall-bounded turbulent flows. This flow phenomenon is well known as Toms effect or drag reduction effect. Rheological drag reduction is promising in applications such as crude oil pipelines and direct heating and cooling systems from an energy-saving perspective. Numerous experimental and numerical studies on drag-reducing wall-bounded turbulent flows of viscoelastic fluids have been reported. However, turbulence structures behind a bluff body have not yet been well investigated. In this study, we investigate turbulence structures in the wake of a wall-mounted finite square cylinder in the flat-plate turbulent boundary layer of viscoelastic fluids using PIV measurements and direct numerical simulations.

INTRODUCTION

Some kinds of polymer and surfactant solutions have viscoelastic properties and often cause significant frictional drag reduction in wall-bounded turbulent flows. This flow phenomenon is well known as Toms effect or drag reduction effect. Rheological drag reduction is quite useful and promising in applications such as crude oil pipelines and direct heating and cooling systems from an energy-saving perspective (Gyr and Bewersdorff, 1995). Numerous experimental and numerical studies on drag-reducing wall-bounded turbulent flows of viscoelastic fluids have been reported. Recently, direct numerical simulation (DNS) studies based on constitutive equation models such as the finitely extensible nonlinear elastic-Peterlin (FENE-P) model (Bird et al., 1987) for drag-reducing wall-bounded turbulent flows of viscoelastic fluids have been performed to demonstrate many experimental findings, such as the steeper gradient in the mean velocity profile in wall-units and greater suppression of turbulence statistics and structures with increasing the drag reduction (see e.g., Tamano et al., 2011, 2018). However, turbulence structures behind a bluff body, which is often installed in practical piping systems, have not yet been well investigated in drag-reducing turbulent flows, unlike Newtonian fluids (see e.g., Yauwenas et al., 2019).

In this study, we perform experimental and numerical studies on turbulence structures in the wake of a wall-mounted finite square cylinder in the flat-plate turbulent boundary layer of viscoelastic fluids using PIV measurements and the corresponding direct numerical simulations, respectively.

EXPERIMENTAL OUTLINE

A closed-loop water tunnel equipped with an acrylic channel (3000 mm × 400 mm × 400 mm) was used. Tap water was circulated by a centrifugal pump to provide a freestream velocity of U_e = 300 mm/s. The water temperature was maintained at 20 ± 0.3 °C using a chiller. A test plate (2798 mm × 387 mm × 20 mm) was mounted vertically on the channel bottom (see Fig. 1). A wall-mounted slit was inclined at 30° to the streamwise direction and was installed 400 mm downstream from the leading edge. The polymer solution was injected at a constant flow rate of 1.04×10^{-2} L/s using a PC-controlled syringe pump. The polymer solution was prepared by dissolving polyethylene oxide (PEO, average molecular weight: 8×10^6 g/mol, Sigma-Aldrich Co. LLC) in purified water at a concentration of 1000 ppm, following the previous study of Shah and Yarusevych (2020).

The coordinate origin was set at the center of the square cylinder base: the streamwise direction was defined as the X-axis, the wall-normal direction as the Y-axis, and the spanwise direction as the Z-axis (see Fig. 1). A square cylinder (the side length of D = 20 mm, height of H = 140 mm, and aspect ratio of $AR \equiv H/D = 7$) was installed 1650 mm downstream from the leading edge at $Z/D = 0$. The Reynolds number was $Re_D \equiv U_e D/\nu = 5980$ (kinematic viscosity $\nu = 1.004 \times 10^{-6}$ m^2/s at 20 °C). The boundary layer thickness at $X/D = 0$ without the square cylinder was δ/H = 0.44. Table 1 shows the main parameters of the experimental and numerical studies.

In the multi-camera PIV measurement, the flow field containing fine tracer particles (KP-010B, particle diameter: 10 μm, specific gravity: 1.03, Kato Koken Co., Ltd.) was captured using four CCD cameras (1600 × 1200 pixels, AM-200 GE, JAI Ltd.) equipped with lenses (AI AF Nikkor 35 mm F/2D, Nikon Corp.). A double-pulse YAG laser (200 mJ/pulse, EverGreen 200, Quantel) and a cylindrical lens generated a 2 mm-thick laser sheet (wavelength: 532 nm) in the *X*–*Y* plane. The cameras and laser were synchronized by a timing controller. The four cameras were arranged in a 2 × 2 array in the streamwise and wall-normal directions (see Fig. 1). The images from the four cameras were merged into a single composite image. For further details on the experimental method, readers are referred to our previous studies (Tamano et al., 2018).

Table 1. Comparison of experimental (Exp.) and numerical (Sim.) conditions in Newtonian fluids.

	Exp.	Sim.
Aspect ratio: AR ($\equiv H/D$)	7	
Reynolds number: Re_D ($\equiv U_eD/\nu$)	5980	1489
Boundary layer thickness: δ/H	0.44	0.81

NUMERICAL OUTLINE

The non-dimensional governing equations for the incompressible viscoelastic flow are the continuity and momentum equations:

$$\frac{\partial u_i^*}{\partial x_i^*} = 0\ , \qquad (1)$$

$$\frac{\partial u_i^*}{\partial t^*} + u_j^* \frac{\partial u_i^*}{\partial x_j^*} = -\frac{\partial p^*}{\partial x_i^*} + \frac{1-\beta}{Re_{\theta_0}} \frac{\partial E_{ij}^*}{\partial x_j^*} + \frac{\beta}{Re_{\theta_0}} \frac{\partial^2 u_i^*}{\partial x_j^* \partial x_j^*}\ . \qquad (2)$$

Here, the superscript * denotes non-dimensional variables scaled by the density ρ, freestream velocity U_e, and momentum thickness at the inlet plane θ_0. t is time, u_i is the velocity component in the x_i direction, p is pressure, and E_{ij} is the viscoelastic stress tensor. $Re_{\theta_0} \equiv \rho U_e \theta_0/\eta_0$ and $\beta \equiv \eta_s/\eta_0$ are the Reynolds number and shear viscosity ratio, respectively. Here, η_s and η_0 are the shear viscosity of the solvent and the zero shear viscosity of the solution, respectively. In the present simulation, Re_{θ_0} was set to 670. β was set to 1.0 and 0.9 for Newtonian and viscoelastic fluids, respectively (Tamano et al., 2011).

The constitutive equation model for viscoelastic stresses is the FENE-P model expressed as follows:

$$\frac{\partial C_{ij}}{\partial t^*} + u_k^* \frac{\partial C_{ij}}{\partial x_k^*} - \frac{\partial u_i^*}{\partial x_k^*} C_{kj} - \frac{\partial u_j^*}{\partial x_k^*} C_{ik} + E_{ij}^* = 0\ , \qquad (3)$$

where C_{ij} is the conformation tensor which satisfies the relation, $E_{ij}^* = (fC_{ij} - \delta_{ij})/Wi$. $f \equiv L^2/(L^2 - C_{kk})$ is the Peterlin function, and $Wi \equiv \lambda U_e/\theta_0$ is the Weissenberg number. λ and L are the relaxation time and maximum polymer extension, respectively. In the present simulation of viscoelastic fluids, Wi and L^2 were set to 30 and 10000, respectively, following our previous study (Tamano et al., 2011). Figure 2 shows the present computational domain and boundary conditions. The coordinate system of X_i (i = 1, 2, 3) is the same as that used in the corresponding experiment. For details on the computational method, readers are referred to our previous studies (Tamano et al., 2011).

RESULTS AND DISCUSSION

Figures 3(a) and 3(b) show the measured contours of instantaneous streamwise velocity u/U_e and instantaneous wall-normal velocity fluctuation v'/U_e, respectively, in addition to the velocity fluctuation vectors (u', v') in the turbulent boundary layer with a square cylinder on the central *X*–*Y* plane (Z/D = 0). The PIV data at X/D = 5.0 and 15.0 are presented for Newtonian fluids ((a–1), (b–1)) and viscoelastic fluids ((a–2), (b–2)). For water, numerous turbulent structures are observed, and upward and downward fluid motions appear periodically and persist downstream. The active turbulence region gradually narrows downstream. For polymer solutions, similar structures become thinner and move further away from the wall in the downstream region, compared with those in water.

Figures 4(a) and 4(b) show the contours of mean streamwise velocity and the mean wall-normal velocity ($\bar{u}$ and $\bar{v}$), respectively, and the streamlines on the central *X*–*Y* plane (Z/D = 0) for the Newtonian case ((a–1), (b–1)) and the viscoelastic case ((a–2), (b–2)) at X/D = 5.0 and 15.0. The saddle point (Wang and Zhou, 2009), defined as a point where the velocity converges in one direction and diverges in the other, is indicated by a white cross. For the Newtonian case, a saddle point is formed immediately downstream of the square cylinder. Above the saddle point, the flow is directed toward the wall, whereas below the saddle point, the flow is directed away from the wall. For the viscoelastic case, the saddle point shifts downstream and farther away from the wall compared with the Newtonian case. For the viscoelastic case, moreover, a relatively high-speed flow region appears near the wall, and the upward flow is distributed over a wider region in the streamwise direction. This behavior is likely attributed to the higher concentration of the injected PEO solution near the wall, where the viscoelastic effects become more pronounced. In the near-wall region, the viscoelasticity would promote the inflow of high-speed fluid toward the central *X*–*Y* plane (Z/D = 0). As a result, the active turbulence region observed in Fig. 3 may be shifted away from the wall.

Figures 5(a) and 5(b) show the iso-surfaces of the Q-criterion (the second invariant of the instantaneous velocity gradient tensor) for Newtonian and viscoelastic fluids, respectively, obtained by DNS. For Newtonian fluids, many fine vortices are generated immediately behind the square cylinder. For viscoelastic fluids, on the other hand, fine vortices behind the square cylinder are strongly suppressed compared with Newtonian fluids, and the relatively large-scale distorted vortices are observed intermittently. In the far downstream region (X/D > 20), large-scale distorted vortices collapse, and vortices are stretched in the streamwise direction. The behavior of large-scale vortex formation and vortex collapse in viscoelastic fluids resembles the results of previous DNS of turbulent planar wakes by Guimarães et al. (2022).

Figures 6(a) and 6(b) show contours of turbulent kinetic energy $K = \overline{u_i'u_i'}/2$ on (a) the central *X*–*Y* plane (Z/D = 0) and (b) the mid-height *X*–*Z* plane (Y/D = 3.5, Y/H = 0.5), respectively. For Newtonian fluids (Figs. 6(a–1) and 6(b–1)), the region where turbulent kinetic energy is dominant is in the vicinity of the square cylinder. For viscoelastic fluids (Figs. 6(a–2) and 6(b–2)), on the other hand, turbulent kinetic energy is strongly suppressed around the square cylinder, and the region where turbulent kinetic energy is dominant forms further downstream compared to Newtonian fluids. Additionally, the peak value of turbulent kinetic energy in viscoelastic fluids is much smaller than that in Newtonian fluids.

Figures 7(a) and 7(b) show contours of the trace of the instantaneous conformation tensor C_{kk}/L^2 on (a) the central X–Y plane ($Z/D = 0$) and (b) the mid-height X–Z plane ($Y/D = 3.5$, $Y/H = 0.5$), respectively. The trace of the conformation tensor C_{kk} represents the degree of polymer extension. Around the square cylinder, the polymer is highly extended. In the downstream region on the mid-height X–Z plane ($Y/D = 3.5$ and $Y/H = 0.5$), the polymer extension region forms regular spatial structures that seem to correspond to the area of relatively large-scale loop vortices (cf. Fig. 5(b)).

CONCLUSIONS

In this study, we performed multi-camera PIV measurements using four synchronized CCD cameras and the corresponding DNS with the FENE-P model to investigate turbulence structures in the wake of the wall-mounted finite square cylinder for the flat-plate turbulent boundary layer flow due to the injection of drag-reducing polymer solutions. The present PIV measurements revealed that upward and downward fluid motions for the polymer injection periodically appear in the downstream region similar to those in water, and such flow structures become thinner and moved further away from the wall compared to water. The present DNS revealed that fine vortices behind the square cylinder were suppressed and several large-scale loop vortices appeared in the downstream region for viscoelastic fluids, where the polymer extension region formed the corresponding spatial structures.

ACKNOWLEDGMENTS

This study was financially supported by the JSPS KAKENHI Grants (JP15H03918, JP23H01342).

REFERENCES

Bird, R. B., Armstrong, R. C., and Hassager, O., 1987, "Dynamics of Polymeric Liquids. Volume 1: Fluid Mechanics", 2nd ed., Wiley Interscience, New York.

Guimarães, M. C., Pinho, F. T., and da Silva, C. B., 2022, "Turbulent Planar Wakes of Viscoelastic Fluids Analysed by Direct Numerical Simulations", *Journal of Fluid Mechanics*, Vol. 946, A26.

Gyr, A., and Bewersdorff, H.-W., 1995, "Drag Reduction of Turbulent Flows by Additives", Kluwer Academic, Dordrecht, The Netherlands.

Shah, Y., and Yarusevych, S., 2020, "Streamwise Evolution of Drag Reduced Turbulent Boundary Layer with Polymer Solutions", *Physics of Fluids*, Vol. 32, 065108.

Tamano, S., Graham, M. D., and Morinishi, Y., 2011, "Turbulent Drag Reduction of Boundary Layer Flow with Non-ionic Surfactant Injection", *Journal of Fluid Mechanics*, Vol. 749, pp. 367–403.

Tamano, S., Uchikawa, H., Ito, J., and Morinishi, Y., 2018, "Streamwise Variations of Turbulence Statistics up to Maximum Drag Reduction State in Turbulent Boundary Layer Flow due to Surfactant Injection", *Physics of Fluids*, Vol. 30, 075103.

Wang, H. F., and Zhou, Y., 2009, "The finite-length square cylinder near wake", *Journal of Fluid Mechanics*, Vol. 638, pp. 453–490.

Yauwenas, Y., Porteous, R., Moreau, D. J., and Doolan, C. J., 2019, "The Effect of Aspect Ratio on the Wake Structure of Finite Wall-mounted Square Cylinders", *Journal of Fluid Mechanics*, Vol. 875, pp. 929–960.

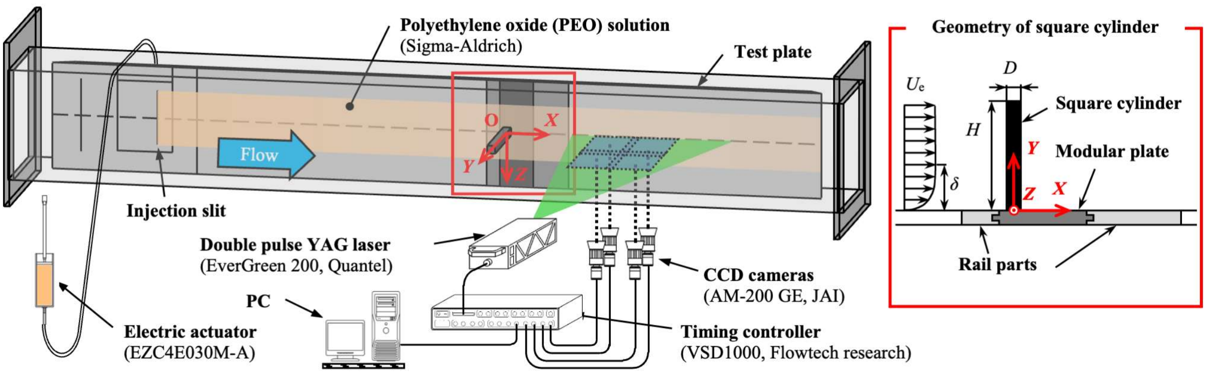

Figure 1. Schematics of experimental apparatus, PIV measurement system, and square cylinder geometry. The experimental apparatus includes the electric actuator and test plate. PEO solution is injected through the injection slit using the electric actuator.

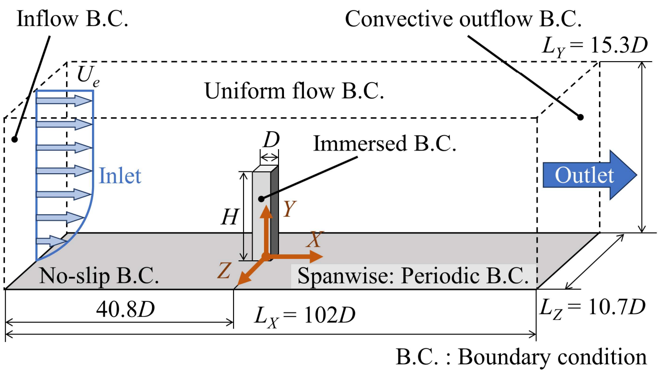

Figure 2. Computational domain and boundary conditions for the boundary-layer flow with a square cylinder.

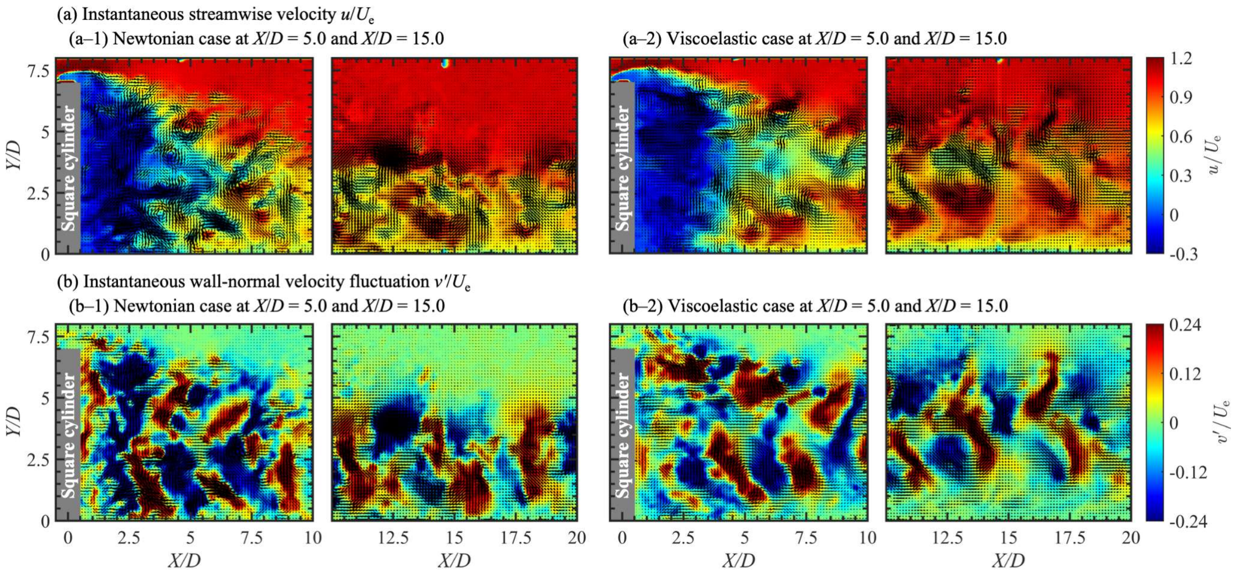

Figure 3. Instantaneous contours and velocity fluctuation vectors (u', v') in the turbulent boundary layer with a square cylinder on the central X–Y plane ($Z/D = 0$): (a) instantaneous streamwise velocity u/U_e and (b) instantaneous wall-normal velocity fluctuation v'/U_e. The results are shown for the Newtonian case ((a–1), (b–1)) and the viscoelastic case ((a–2), (b–2)) at X/D = 5.0 and 15.0.

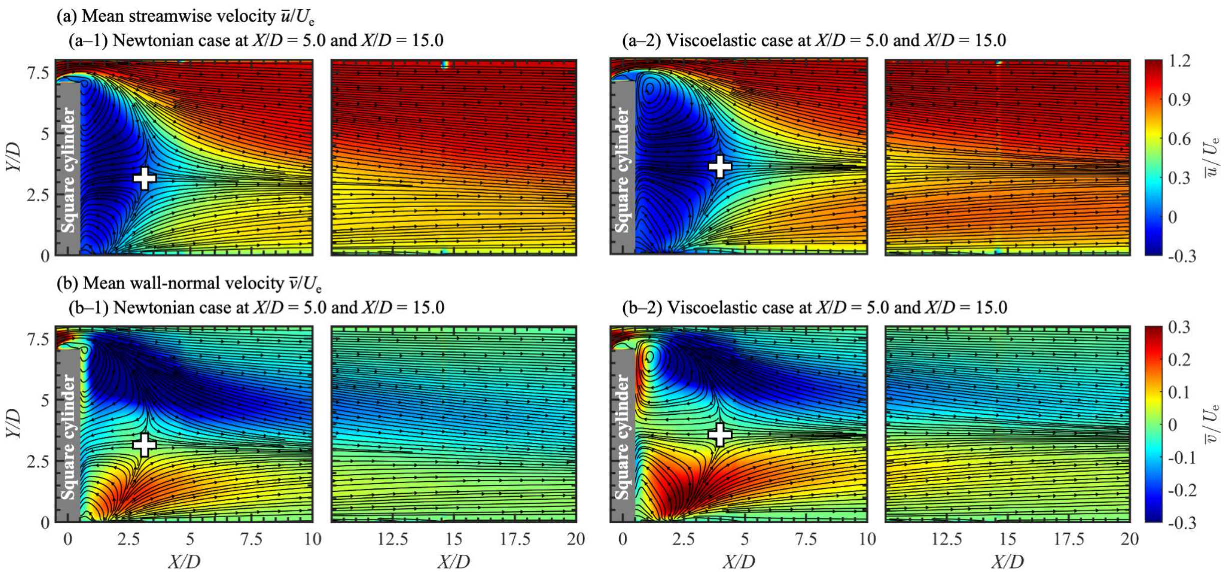

Figure 4. Contours of time-averaged velocity ($\overline{u}$, $\overline{v}$) and streamlies in the turbulent boundary layer with a square cylinder on the central X–Y plane ($Z/D = 0$): (a) mean streamwise velocity $\overline{u}/U_e$ and (b) mean wall-normal velocity fluctuation $\overline{v}/U_e$. The results are shown for the Newtonian case ((a–1), (b–1)) and the viscoelastic case ((a–2), (b–2)) at X/D = 5.0 and 15.0. The saddle point, defined as a point where the velocity converges in one direction and diverges in the other, is indicated by a white cross.

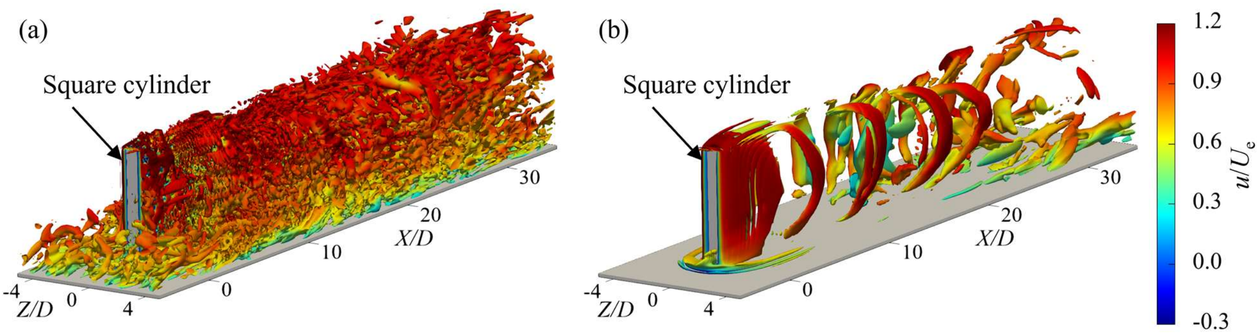

Figure 5. Iso-surfaces of the second invariant of the instantaneous velocity gradient tensor $QD^2/U_e^2 = 0.03$ obtained by DNS for (a) Newtonian fluids and (b) viscoelastic fluids. The colormap represents the instantaneous streamwise velocity U/U_e.

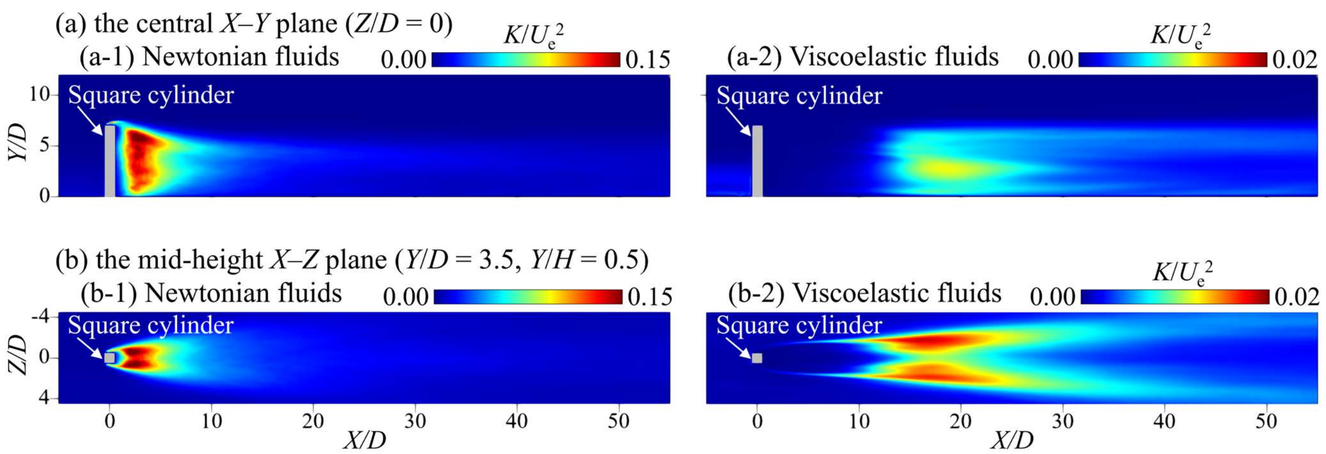

Figure 6. Contours of turbulent kinetic energy $K = \overline{u_i'u_i'}/2$ on (a) the central X–Y plane ($Z/D = 0$) and (b) the mid-height X–Z plane ($Y/D = 3.5$, ($Y/H = 0.5$)), respectively, for Newtonian fluids (Figs. 6(a–1) and 6(b–1)) and viscoelastic fluids (Figs. 6(a–2) and 6(b–2)).

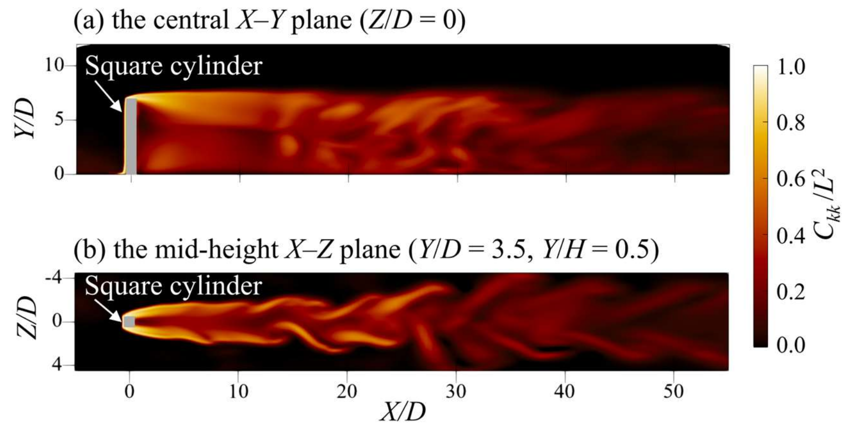

Figure 7. Contours of the trace of the instantaneous conformation tensor C_{kk}/L^2 on (a) the central X–Y plane ($Z/D = 0$) and (b) the mid-height X–Z plane ($Y/D = 3.5$, $Y/H = 0.5$), respectively.